

MICROSTRUCTURAL CHARACTERIZATION OF ENERGETIC MATERIALS

LA-UR – 02-2920

P. D. Peterson, J. T. Mang, S. F. Son, B. W. Asay, M. F. Fletcher, R. P. Hjelm, and E. L. Roemer
Los Alamos National Laboratory, Los Alamos, NM 87545, USA
pdp@lanl.gov

ABSTRACT

It is well known that microstructural features, such as defect and crystal morphology, and size distribution may dramatically affect ignition sensitivity and performance characteristics of energetic materials. The quantification of these microstructural features is therefore essential to the construction of full-scale constitutive models for both pristine and damaged materials.

As these microstructural features occur across a wide range of length scales (from nanometers to millimeters) a variety of techniques are needed to elucidate these features. For large length scales (1 μm -10mm), polarized light microscopy (PLM) provides information about material microstructure and defects. At the intermediate length scales (10 nm – 1 mm), similar features can be studied using scanning electron microscopy (SEM).

For the smallest length scales (0.1 nm – 1 μm) techniques such as small-angle x-ray scattering (SAXS), and small-angle neutron scattering (SANS) are required in order to obtain a more complete description of microstructural features. SANS and SAXS are unique in their ability to quantitatively determine fine details of structure such as particle morphology and size at length scales from nanometers to microns in a wide range of materials. In addition SANS and SAXS can be used to probe composite structures containing crystals, binder, and voids, or metals and oxide layers. Unlike transmission electron microscopy (TEM) methods in which size distributions and morphology from statistically small samples must be extrapolated to the bulk materials, these scattering techniques can be used to probe the entire bulk sample.

In order to characterize energetic material microstructure, we have used these diagnostic techniques to examine a variety of energetic materials in pristine and damaged states across a wide range of length scales. The materials include: PBX 9501 (pristine, physically damaged, and thermally damaged) and energetic nano-materials.

INTRODUCTION

Minor differences in microstructure can lead to dramatic changes in the performance of energetic materials. For example, typical thermite materials (micron scale) burn at centimeters per second, while nanoscale superthermite powders can propagate at a rate on the order of thousands of meters per second. In classical energetic materials microstructural differences may be induced in formulation and processing, or generated by physical insult, chemical insult, or aging. Detecting and understanding these differences requires the ability to probe microstructural features with sizes ranging from millimeters to angstroms. As no one characterization method can cover this entire range of length scales, a variety of techniques must be incorporated.

In order to span the entire range of length scales we are using characterization techniques including polarized light microscopy (PLM), scanning electron microscopy (SEM), and small-angle scattering (SAS). In combination, these techniques allow us to quantitatively identify features and differences in materials over length scales from 10^{-10} to 10^{-2} meters.

Here, we present a brief description of these three techniques and examples of their application to four current projects related to energetic materials. These projects include characterization of the microstructure of pristine PBX 9501, changes in particle size of PBX 9501 due to differences in pressing intensity during formulation, changes in the PBX 9501 microstructure due to a linear thermal gradient and morphological differences within nano-scale metastable intermolecular composites (MIC) materials, in particular Al/MoO₃ composites.

METHODS

Polarized Light Microscopy (PLM)

In order to probe relatively large features (1 μ m-10mm) of energetic materials, we are currently using a Lieca DM-RXA polarizing light microscope along with a Diagnostic Instruments SPOT 100 camera that provides high resolution (1315 x 1033 pixels) digital micrographs

Historically, one of the inherent weaknesses of PLM has been the qualitative nature of the results. To extract quantitative details from the PLM images, image processing routines must be used. We are currently using routines written using Clemex Vision™ image analysis software. These routines incorporate image color thresholding and geometric constraints to quantitatively determine specimen characteristics such as area percentages and crystal size distributions.

For all PLM samples, preparation is quite extensive, and critical to achieving good results. Typical sample preparation requires cutting the energetic specimens, potting the specimens in epoxy, and polishing. A 125 mm diameter aluminum oxide cut-off wheel at 1000 rpm is used for cutting. The specimen is then potted in Struers Epofix 2 part epoxy under vacuum (500 mbar) and then pressurized under nitrogen (500 psi). After allowing the epoxy to dry under pressure overnight, the specimen is removed from the pressure cell and the face of interest is polished to a smooth finish using a Struers Rotapol-25/Pedemin_S automatic grinding/polishing machine. Polishing materials include SiC polishing papers (1200 grit, 2400 grit, 4000 grit), Al₂O₃ polishing powders (1 μ m and 0.3 μ m), and an OP-S suspension (0.03 μ m). A typical image of PBX 9501 is shown in Figure 1.

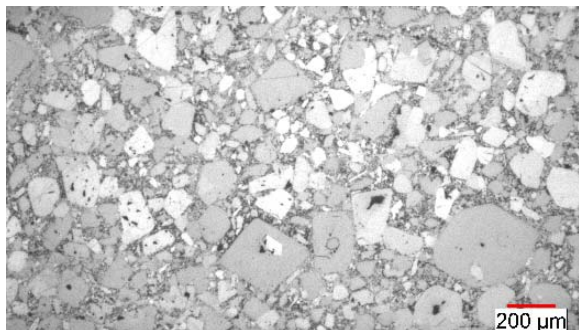


Figure 1) PLM micrograph of PBX 9501

Scanning Electron Microscopy (SEM)

Scanning Electron Microscopy (SEM) can be used to probe microstructural features from 10 nm – 1 mm. We have recently acquired a Field Emission Scanning Electron Microscope (FESEM). The FESEM allows imaging of many non-conductive materials at relatively low voltages (200 eV – 30 keV) without applying a conductive coating. In addition, we have purchased both an energy dispersive x-ray spectrometer (EDS) and a wavelength dispersive x-ray spectrometer (WDS), which allows analysis, quantification, and mapping of elements. Typical SEM images of PETN and nano-aluminum (both uncoated) are shown in Figures 2 and 3.

Small Angle Scattering (SAS)

We are currently using both Small Angle Neutron Scattering (SANS) and Small Angle X-ray Scattering to characterize length scales from 0.1 nm – 1 μm within energetic materials. In a SAS experiment, a beam of neutrons or x-rays impinges upon a sample characterized by a scattering length density, $\rho(\mathbf{r})$, which reflects the microscale structure (see Fig. 4). Fluctuations in $\rho(\mathbf{r})$ give rise to small-angle scattering. The intensity of the scattered radiation, $I(Q)$, is measured as a function of

the scattering vector, \mathbf{Q} , of magnitude $Q = (4\pi/\lambda)\sin\theta$, where λ is the wavelength of the

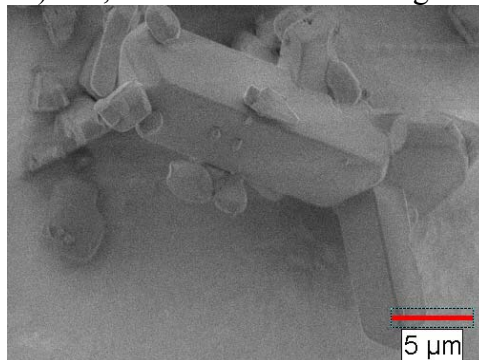


Figure 2) SEM of PETN crystals

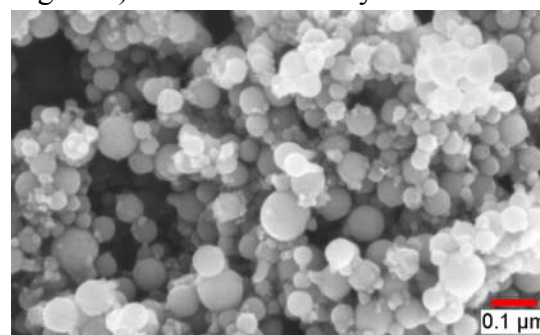


Figure 3) SEM of Nano aluminum

incident radiation and θ is half of the scattering angle. $I(Q)$, for a monodisperse system of non-interacting particles, dispersed in a uniform media, can be expressed as¹,

$$I(Q) = N\Delta\rho^2 V^2 \langle P(Q) \rangle \quad (1)$$

where $P(Q)$ is the normalized, single particle form (shape) factor and is related to Fourier transform of $\rho(\mathbf{r})$, V is the particle volume, and N is the number of scatterers per unit volume. Also, $\Delta\rho$ is the scattering length density contrast between the average scattering length density of the particle, and that of the surrounding media. The complete interpretation of $I(Q)$ in terms of the sample structure, $\rho(\mathbf{r})$, ultimately involves careful comparison with calculations of the scattering expected from model structures.

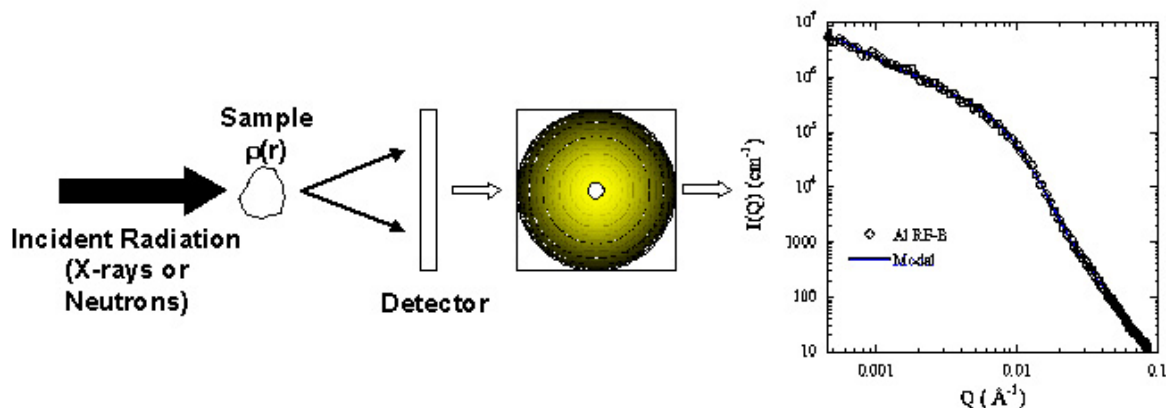


Figure 4) Schematic of small-angle scattering technique

An advantage of SANS and SAXS is that a statistically significant number of particles is sampled in a single measurement, which allows accurate assessment of particle size distributions. For the studies outlined in this paper, SANS measurements were performed on the Low-Q Diffractometer (LQD) at the Manuel Lujan Jr., Neutron Scattering Center at Los Alamos National Laboratory ². SAXS measurements have been made at the University of New Mexico ³. In both cases, data were reduced by conventional methods and corrected for empty cell and background scattering. Absolute intensities were obtained by comparison to a known standard and normalization to sample thickness.

STUDIES

PLM, SEM, and SAS techniques used in combination can effectively characterize material microstructure across the entire range of length scales from 10^{-10} to 10^{-2} meters (Figure 5). Differences in microstructure between pristine and damaged energetic materials can then be related to changes in mechanical properties and material performance. A variety of energetic materials are currently being characterized using these microstructural techniques. In what follows, we discuss current studies of pristine and physically and

thermally damaged PBX 9501 and Metastable Intermolecular Composites (MIC).

Pristine PBX 9501

PBX 9501 is formulated using 92.7/7.2 vol% HMX(3:1 class 1,2) / Estane-BDNPA-F binder. Sieve sizes for the different classes of HMX are shown in Table 1. Figure 6 shows an image of pristine PBX 9501 taken at a magnification of 50X using the PLM. Although the specified pre-pressed crystal size distribution indicates that 37% of the crystals will be smaller than $44 \mu\text{m}^2$ (3:1 class 1,2), crystal fracture during pressing will result in a smaller average crystal size.

Table 1. Sizes for some HMX classes.		
Max Area (μ^2)	% Class 1	% Class 2
297	90 ± 6	100
149	50 ± 10	--
125	--	> 98
74	20 ± 6	--
44	8 ± 5	> 75

Figure 7 shows the same image after it has been characterized using routines written in Clemex Vision. The HMX crystals have been labeled yellow and dirty binder regions (binder, voids, and crystals

smaller than $0.8\mu\text{m}^2$) labeled in dark blue. Outside edges of the image have been excluded from the analysis to avoid counting incomplete edge crystals. As the PLM images are necessarily two-dimensional, approximate size distributions are reported in terms of area and are consequently conservative. At this magnification, crystals larger than $0.8\mu\text{m}^2$ will be detected.

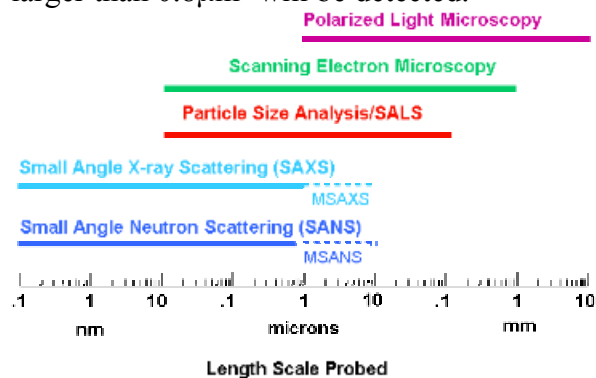


Figure 5) Microstructure Characterization Techniques for Energetic Materials

Results of the image analysis at a magnification of 50X indicate that the specimen contains 73.1 area% HMX and 26.9 area% dirty binder. A similar analysis of dirty binder regions at higher magnification (400X) indicates that the dirty binder contains approximately 62% HMX (crystals of size $0.8\text{-}0.05\mu\text{m}^2$) as shown in Figures 8 and 9. This suggests an overall percentage of 89.7% HMX crystals, which is approaching the theoretical value. A statistical analysis of 10 separate images from two independent specimens gives a average crystal area% of 90.3 ± 0.5 vol% with 67% of the crystals being smaller than $0.8\mu\text{m}^2$.

These results suggest that pressed pellets of PBX 9501 contain dramatically different crystal morphology and size distributions than the pre-pressed molding powder⁴.

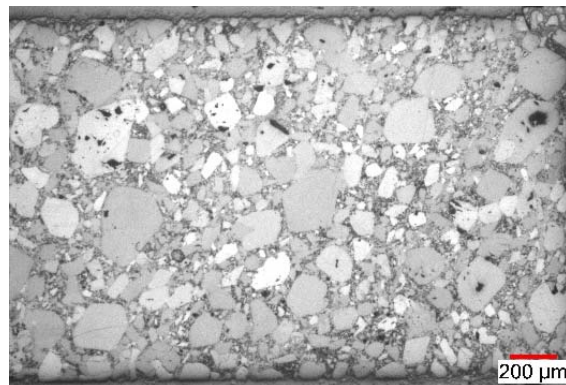


Figure 6) PLM of PBX 9501 (50X)

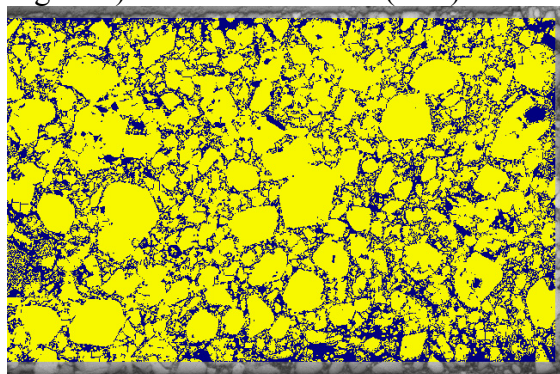


Figure 7) Analysis of PBX 9501 (50X)

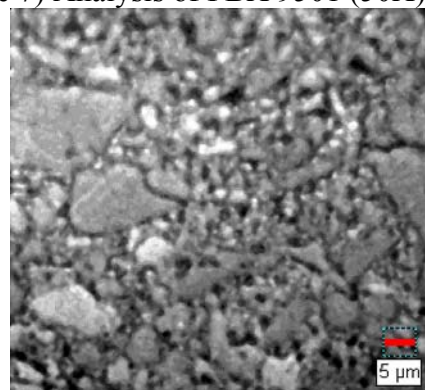


Figure 8) PLM of PBX 9501 (400X)

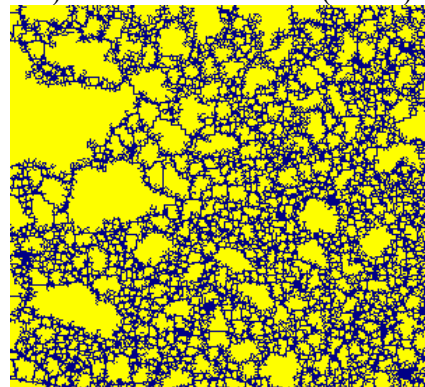


Figure 9) Analysis of PBX 9501 (400X)

Mechanically-Damaged PBX 9501

In the preparation of PBX 9501 samples, pressing conditions are often varied in order to achieve nominal density. Although density is met, differences in pressing intensity, or procedures (sometimes pressure is released and then reapplied, for example), can lead to variations in microstructure between samples due to crystal fracture. To evaluate the effect of pressing intensity on the microstructure, three cylinders (1" ϕ x 1" long) of PBX 9501 (HOL Lot 89C730-010 MT 345) have been pressed at 5,000 psi, 15,000 psi, and 30,000 psi, respectively, using a 50 Ton press. Following pressing, the entire profile of each cylinder has been examined for microstructural changes due to the different pressing conditions. Both polarized light microscopy and small-angle x-ray scattering (SAXS) techniques have been used to probe the particle morphology, porosity, crystal size and size distribution of each cylinder.

After pressing, each of the three cylinders was sectioned twice, along the centerline, using a diamond anvil saw. A total of 18 pieces were then cut from the two resulting sections as shown in Figure 10.

For each cylinder, pieces 1-9 were analyzed for microstructural differences using polarized light microscopy. These nine pieces had approximate dimensions of 0.3" x 0.3" x 0.15". Each of these pieces was prepared for PLM characterization as outlined before. Pieces 10-18 from each cylinder had approximate original dimensions of 0.3" x 0.3" x 0.05" and were polished to a thickness of 0.03" using 1 μ m Al₂O₃ polishing powder. These pieces were analyzed using SAXS.

Photomicrographs of the center of region 5 of each of the samples are shown in Figures 11-13 respectively. Qualitative differences in microstructure are clear across the three images. At 5,000 psi (Figure 11),

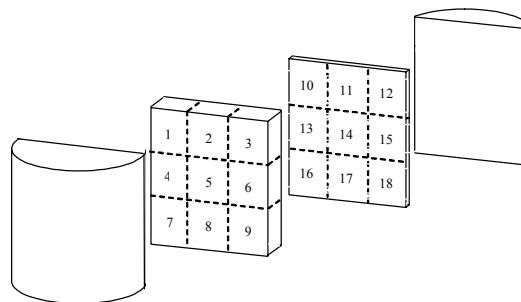


Figure 10) Specimen preparation and orientation

in general, the crystals appear to be well segregated from each other by binder. This cushioning effect protects the crystals from fracturing due to crystal-crystal contact forces. Some fine crystals can be seen within the binder, however even these appear to be fairly dispersed (Figure 14). At 15,000 psi (Figure 12) many of the crystals in the image have been pressed into contact with each other. At the points of contact, crystal fracture and rubblization has occurred (Figure 15). In addition, much of the binder material appears lighter due to the generation of more fine crystals. At 30,000 psi, increased rubblization due to crystal contact and fracture has occurred and more fine crystals are visible in the binder rich regions (Figure 16).

Image analysis techniques were used to further analyze PLM images from 5 different points within regions 1 and 5 from each specimen. Five random PLM images were taken from each region and compared with the corresponding region from the other pressed cylinders. Each image was analyzed for differences in crystal size as a function of specimen location and pressing intensity. Figure 17 shows a plot of the average particle sizes within regions 1 and 5 from each cylinder. Five data points, one from each image, are shown for each region.

The results indicate that for crystals larger than 0.8 μ m² in area, a majority of the

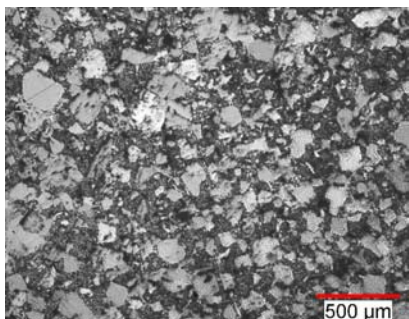


Figure 11) PBX 9501
5,000 psi, 1.7976 g/cc

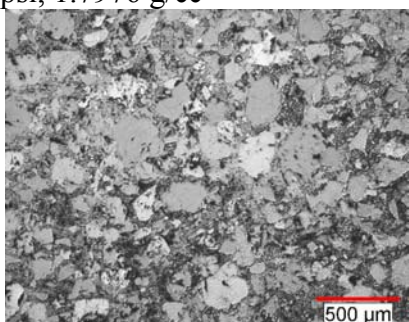


Figure 12) PBX 9501
15,000 psi, 1.8294 g/cc

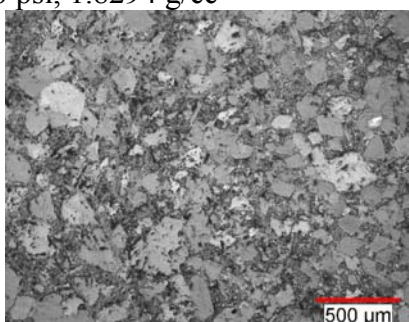


Figure 13) PBX 9501
30,000 psi, 1.8342 g/cc

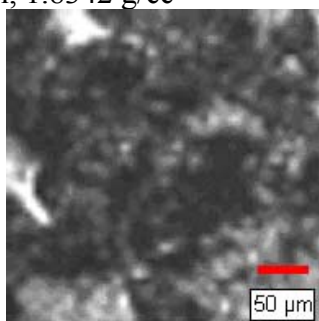


Figure 14) Binder containing few crystals

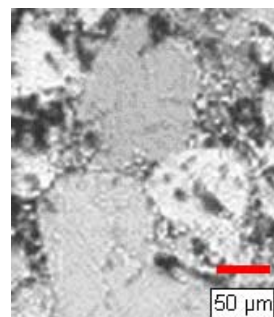


Figure 15) Crystal rubblization at point of contact

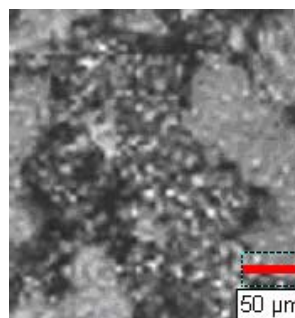


Figure 16) Increased number of fine crystals in binder rich areas

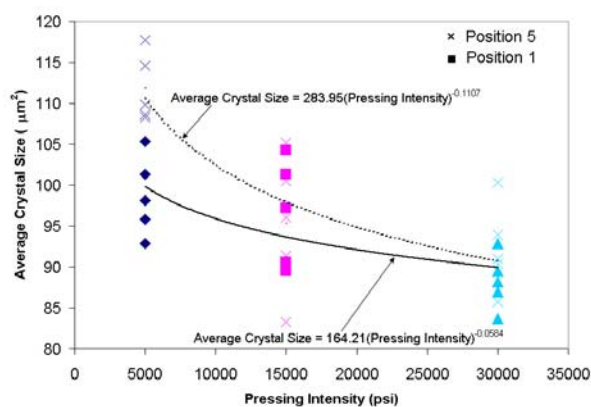


Figure 17) PLM--Average Crystal Size

crystal damage and fracture occurs along the outside edges of the specimen at pressures below 5,000 psi. At intermediate pressures, (between 5,000 psi and 15,000 psi) a majority of the damage occurs at the center of the specimen. As pressing intensity increases above 15,000 psi there is only a small change in the average crystal size, considering only crystals larger than $0.8\mu\text{m}^2$.

Figure 18 displays a Log-Log plot of the SAXS data obtained from region 10 at different applied pressures, where the data

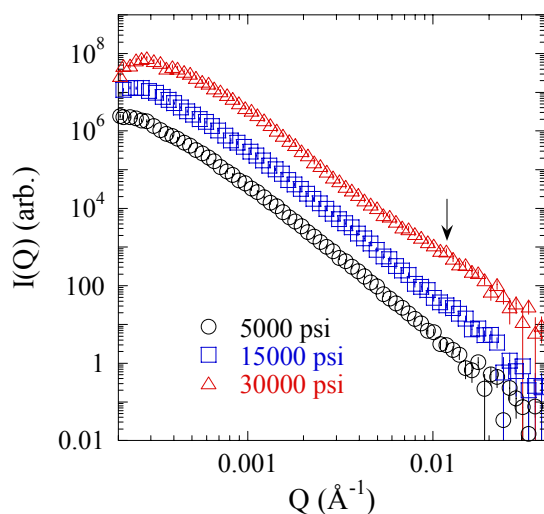


Figure 18) SAXS – Pressing-induced microstructural changes

have been shifted along the vertical axis for clarity. The measured curves measured at 5000 and 15,000 psi have the same shape, indicating that there are no significant changes in the microstructure, at the length scales probed by SAXS, caused by the increased pressure. However, we see a new feature in the data obtained from the sample pressed at 30,000 psi. The appearance of a “knee”, centered at $Q = 0.013 \text{ \AA}^{-1}$ (as indicated by the arrow), corresponds to the presence of a new distribution of particles, having an average diameter of $\sim 800 \text{ \AA}$. This is consistent with the notion of increased rubblization of the large HMX crystals.

Thermally Damaged PBX 9501

PBX 9501 has also been subjected to a linear thermal gradient in order to study the physical and chemical changes that occur due to heating. Three separate cylinders (5 mm diameter by 72mm length) were placed in a brass sample holder. Brass end caps were placed at both ends of the specimen. Thermocouples were inserted along the length of the specimen to monitor the temperature distribution as shown in Figure 19. The end-caps were then heated

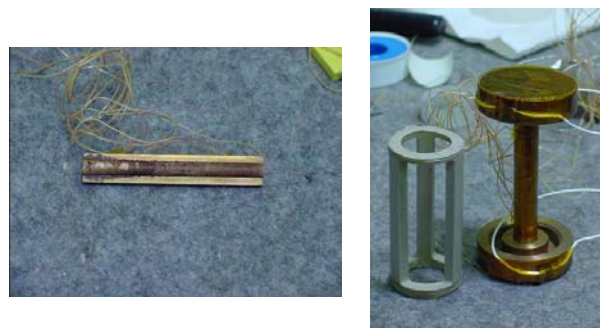


Figure 19) Setup for Linear Thermal Damage Tests

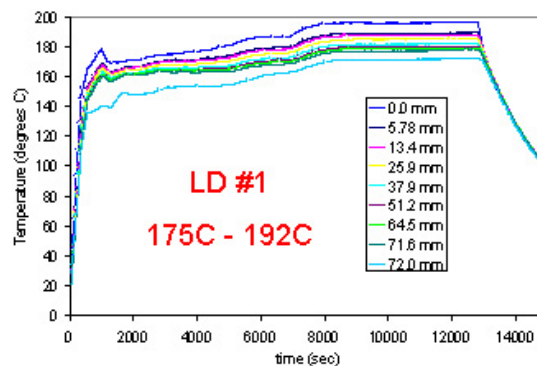


Figure 20) Heating Profile for Test 1

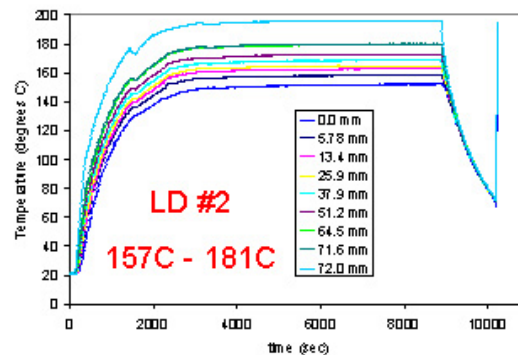


Figure 21) Heating Profile for Test 2

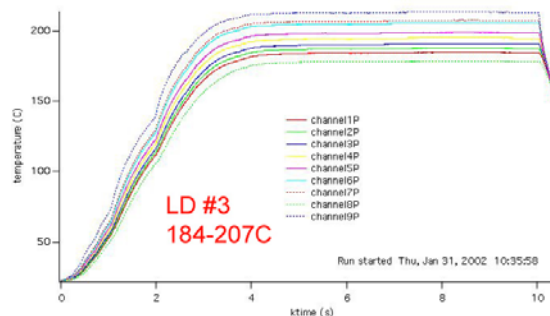


Figure 22) Heating Profile for Test 3

to specified temperatures to produce the desired temperature gradient across the length of the specimen. Each cylinder was heated until a steady-state temperature distribution was established for two hours. Temperature profiles for each of the three specimens are shown (Figures 20-22). After the test, the samples were sectioned down the centerline. Half of each specimen was analyzed with the PLM, while the other half was analyzed using SANS. For the PLM, the samples were cut into quarters, potted, and polished as described previously. Clemex Vision image analysis software was used to analyze the changes in crystal/binder percentage as a function of temperature.

Results of the analysis are shown in Figure 23. The dotted lines indicate the locations where the samples were sectioned as part of the PLM preparation. It should be noted that the third section of Linear Damage Sample #2 contained a tortuous fracture along the centerline of the specimen. As a result, PLM images could not be taken from the centerline. Although slight radial temperature differences may affect the magnitude of the results, the general increasing trend in crystal percentage should be correct.

The results indicate a rapid rise in the overall percentage of crystals between 170C and 175C. Above 175C the overall percentage of crystals slowly decreases until a temperature of approximately 195C. Above 195C the rise in crystal percentage is probably due to an inversion of the crystal and binder coloration as the crystals become darker than the binder material.

Figure 24 displays the results of SANS measurements from the Linear Damage Sample #1. The plot displays the ratio of scattered intensity, measured at several points along the thermal gradient, to a point at the cooler end of the sample. As we can see in the figure, a peak, centered at

$Q \sim 0.015 \text{ \AA}^{-1}$ appears in the plot. The intensity of the peak increases with increasing temperature, indicating the development of thermally induced defects of radius $\sim 200 \text{ \AA}$ in the PBX 9501 microstructure. Further analysis of the SANS data allows a determination of the total surface area per unit volume (S_V) of the sample. Comparing S_V measured at different points along the sample (Fig. 25) to that measured at the coolest end of the sample (S_0) shows a dramatic increase in surface area with increasing temperature. This suggests the presence of thermally induced crack and defect formation throughout the microstructure.

Metastable Intermolecular Composites (MIC)

Engineered nano-scale composite energetic materials, such as Al/MoO₃, have shown promise for energetic material applications because the nanocomposite can react extremely rapidly. Reaction rates are orders of magnitude faster than conventional formulations.² As a consequence these materials have application directly for such things as primers. Nano-materials can also be formulated with other energetic materials, including gas generating materials, and used for a much wider variety of applications. These nanocomposite energetic materials have been historically termed metastable intermolecular composites (MIC). Here we use this term to refer to any energetic material utilizing nanoscale energetic constituents.

Although these materials have been available in the recent years, much work remains to fully characterize their morphology. SEM, SANS, and SAXS are proving to be useful tools to characterize size distribution and oxide layer thickness for these nano-materials. Al and MoO₃

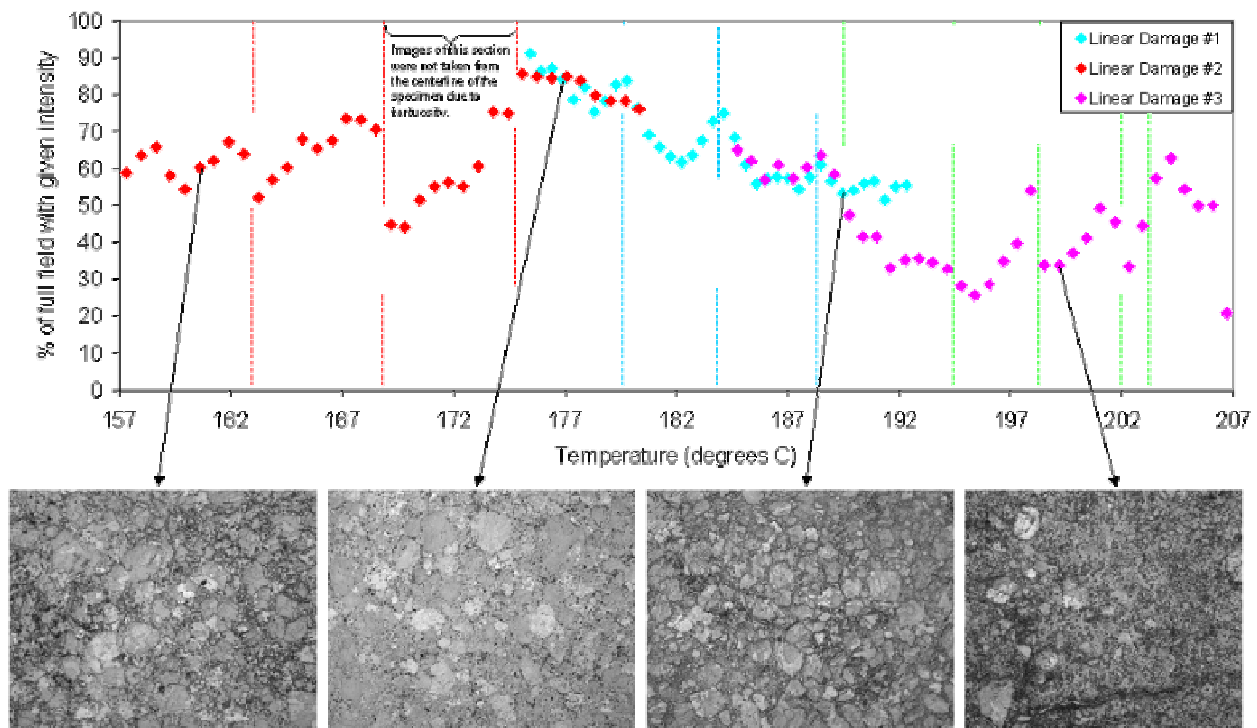


Figure 23) Thermally Induced Damage in PBX 9501 – PLM

powders were characterized using several different techniques to determine the particle size distribution, passivation layer thickness, and degree of particle agglomeration.

Figures 26 and 27 show SEM images of typical aluminum samples. Our experience is that as the average particle size increases, the particle size distribution broadens. Also observed in Fig. 26, we see agglomeration in the form of chains or branches. Similarly, Fig. 28 is MoO_3 and finally Fig. 29 is Al/MoO_3 MIC. The MoO_3 images reveal sheet-like structures, intermixed with aggregates.

SAXS can provide a quantitative measure of sheet thickness for the MoO_3 . Figure 30 shows data obtained from SAXS measurements of a sample of Climax MoO_3 . The solid line in the figure is a result of a fit to a model (developed based upon SEM images) of polydisperse sheet-like structures with large aggregates. As seen in the figure, the model is consistent with the measured

data. An average of 15.5 nm was measured for the sheet-like structures seen in the SEM image (Fig. 28).

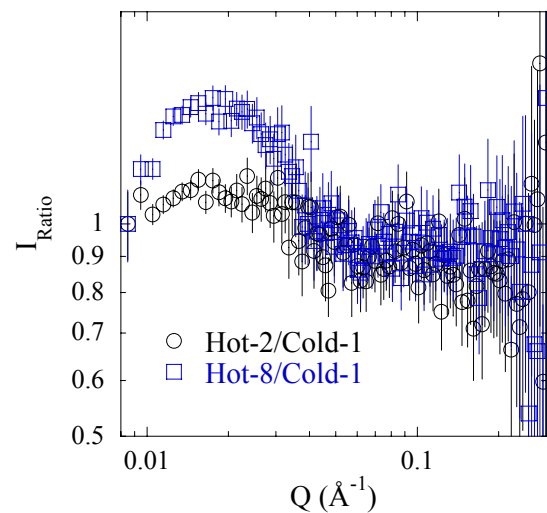


Figure 24) SANS from Linear Damage Sample #1

In Figure 31 we show the distribution obtained from SAXS measurements of three Los Alamos produced nano-aluminums. Based upon the SEM images, a model of mass fractal aggregates was used to interpret the scattering data (see Fig. 26 for example). This model was found to be consistent with the SAXS data. The volume-weighted size distribution obtained from the analysis is shown.

Figure 32 is a comparison of size distributions from different Al powders obtained from a SAXS measurement and TEM images. The comparison is reasonable considering the limitations of the sample size considered in the TEM measurements (only a few hundred particles), possible halo effect (electron diffraction) in the TEM images, and the difficulty determining the diameter of agglomerates.

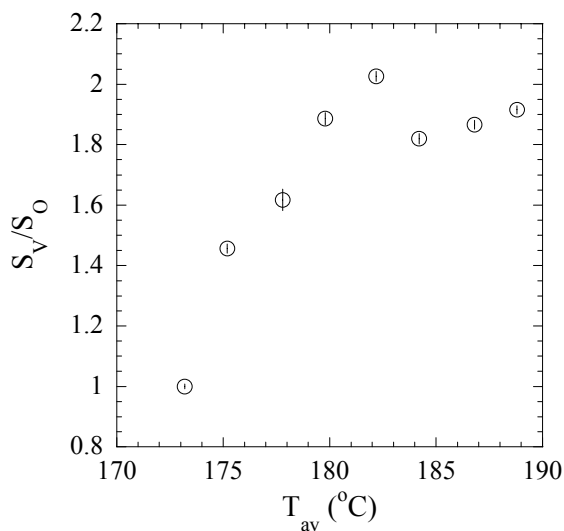


Figure 25) SANS surface area measurement of Linear Damage Sample #1

In contrast, the SAXS measurement includes $\sim 10^{18}$ particles. Table 2 shows sizing results from SAXS with comparisons to other approaches. In Table 2, R_{av} is the average radius, D_{av} is the average diameter, and δ is the oxide layer thickness.

CONCLUSIONS

We have used PLM, SEM, SANS, and SAXS in order to quantitatively characterize microstructural features of pristine and damaged PBX 9501 across the range of length scales from 10^{-10} to 10^{-2} meters. Pressed pellets of PBX 9501 demonstrate different crystal morphology and size distributions than the pre-pressed molding powder. Both pressing conditions and thermal history will also result in microstructural changes within PBX 9501.

SEM, SANS, and SAXS have also been used to study morphological differences within MIC materials and their constituents. SAS provides a much better statistical measure of particle size and morphology than other standard techniques.

REFERENCES

1. Glatter, O. and Kratky, O., *Small Angle X-ray Scattering* (Academic Press, London, 1982).
2. Seeger, P. and Hjelm, R., *J. Appl. Cryst.*, **24**, 467 (1991).
3. Rieker, T. P., Hubbard, P. F., *Review of Scientific Instruments*, **69**, 3504 (1998).
4. Burnside, N., S. F. Son, B. W. Asay, and C. B. Skidmore, *Particle Characterization of Pressed Granular HMX*. in Shock Compression of Condensed Matter. 1997. Amherst MA: AIP

ACKNOWLEDGEMENTS

We acknowledge the support of Los Alamos National Laboratory, under contract W-7405-ENG-36. In particular, we acknowledge the support of the W76 Lifetime Extension Program and DoD/DOE MOU program of Los Alamos National Laboratory. We also acknowledge Harriet Kung for the TEM size measurements.

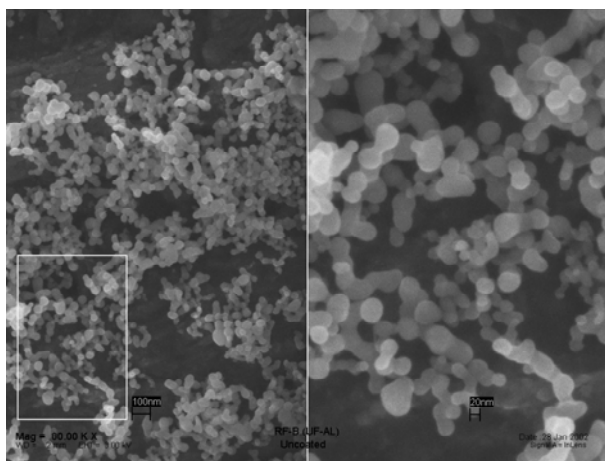


Figure 26) SEM image of nano-aluminum made at Los Alamos, designated RF-B.

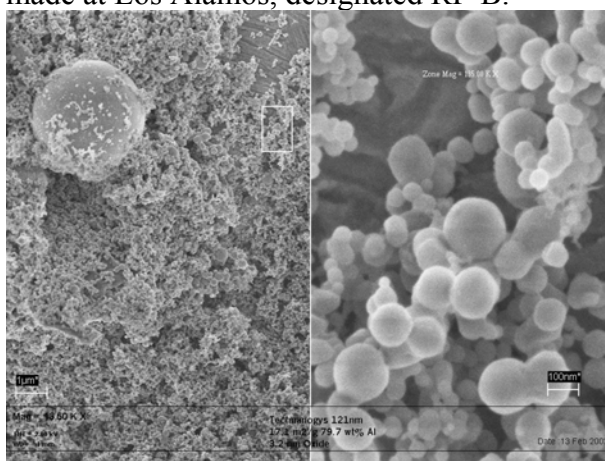


Figure 27) Larger aluminum made by Technanogy, designated Technanogy-121. Technanogy also makes small aluminum powders similar to Figure 26.

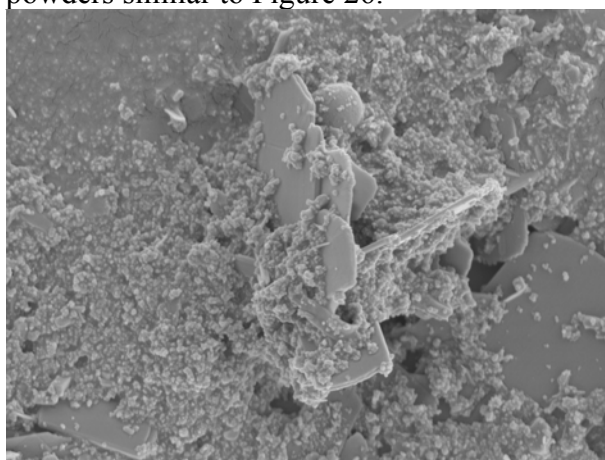


Figure 28) MoO_3 from Climax. Sheet-like material is observed with smaller particles

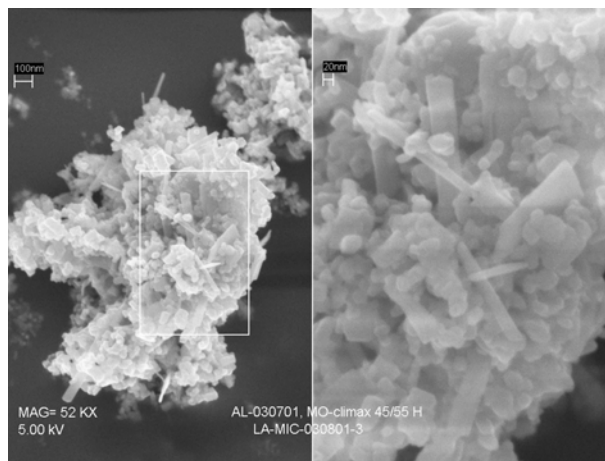


Figure 29) Al/MoO₃ MIC

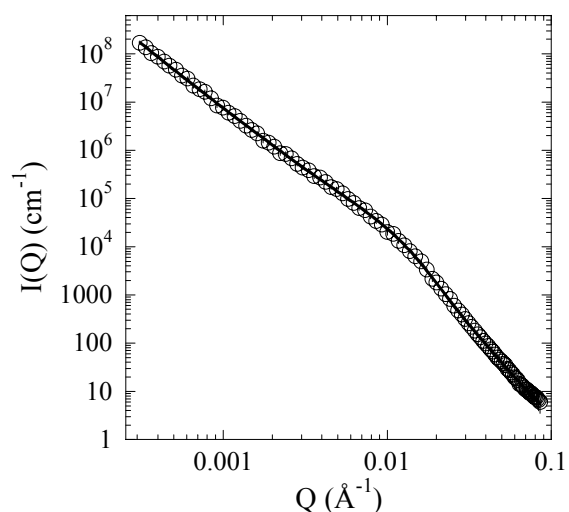


Figure 30) SAXS results obtained from MoO₃.

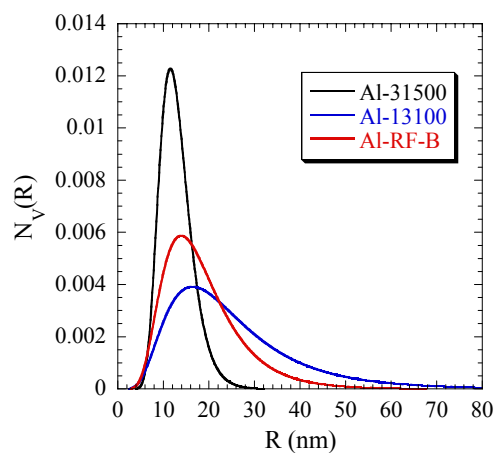


Figure 31) Volume weighted distributions of three Los Alamos aluminum samples.

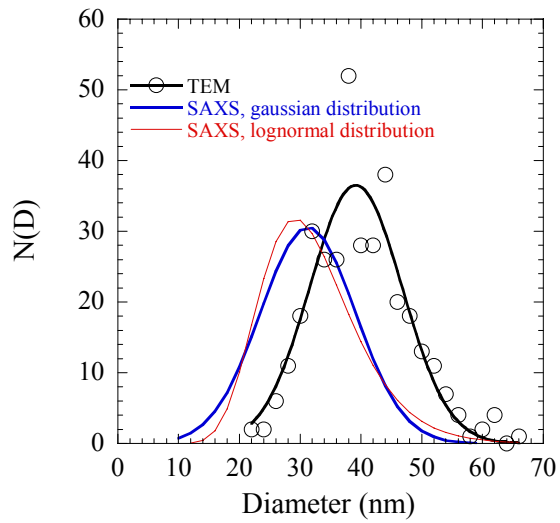


Figure 32) Comparison of size distributions obtained from a SAXS measurement and TEM images.

Table 2) Sizing of aluminum core and oxide layer by various techniques

Powder	Fractal Dim.	RavN R core (nm)	RavN V core (nm)	DavN R (nm)	DavN V (nm)	BET δ_{av} (nm)	δ (nm)	TEM δ (nm)	BET/TGA δ (nm)	Vel δ (nm)
Al-31500	1.98±0.1	10.4±0.1	12.9±0.1	26.2±0.2	31.2±0.2	32.90	2.68 ±0.02	2.83	2.45	2.87
Al-13100	1.7±0.2	10.6±0.2	25.4±0.3	26.1±0.4	54.9±0.6	34.15	2.44 ±0.02	4.62	2.45	2.98
Al RF-B	1.8±0.1	10.4±0.1	18.7±0.1	26.5±0.2	43.1±0.2	-	2.86 ±0.02	-	-	-